ARTICLE

Friction and Adhesion of Hierarchical Carbon Nanotube Structures for Biomimetic Dry Adhesives: Multiscale Modeling

Shihao Hu, Haodan Jiang, Zhenhai Xia,* and Xiaosheng Gao

Department of Mechanical Engineering, University of Akron, Akron, Ohio 44325

ABSTRACT With unique hierarchical fibrillar structures on their feet, gecko lizards can walk on vertical walls or even ceilings. Recent experiments have shown that strong binding along the shear direction and easy lifting in the normal direction can be achieved by forming unidirectional carbon nanotube array with laterally distributed tips similar to gecko's feet. In this study, a multiscale modeling approach was developed to analyze friction and adhesion behaviors of this hierarchical fibrillar system. Vertically aligned carbon nanotube array with laterally distributed segments at the end was simulated by coarse grained molecular dynamics. The effects of the laterally distributed segments on friction and adhesion strengths were analyzed, and further adopted as cohesive laws used in finite element analysis at device scale. The results show that the laterally distributed segments play an essential role in achieving high force anisotropy between normal and shear directions in the adhesives. Finite element analysis reveals a new friction-enhanced adhesion mechanism of the carbon nanotube array, which also exists in gecko adhesive system. The multiscale modeling provides an approach to bridge the microlevel structures of the carbon nanotube array with its macrolevel adhesive behaviors, and the predictions from this modeling give an insight into the mechanisms of gecko-mimicking dry adhesives.

KEYWORDS: carbon nanotube • fiber • friction • adhesion • interface • gecko mimicking • dry adhesives • mechanical properties • molecular dynamics • finite element analysis

1. INTRODUCTION

Geckos can climb and even run vertically or inverted on almost any surface. The extraordinary locomotion ability stems from the universally existed van der Waals interactions between the submicrometer hairs covering geckos' feet and target surfaces (1−3). The structures of gecko's feet have evolved into a multilevel hierarchical system consisting of nearly 500 000 keratinous fibrils called setae and their nanosized branches called spatulae. The van der Waals interactions, acting collectively on each single spatula pad, generate a formidable adhesive strength of ∼10 N/cm^2 (1, 4), regardless of the surface property (hydrophilic or hydrophobic, rough or smooth) of the targets. Mimicking the gecko's footpad structure could lead to a new class of advanced synthetic adhesives, which would be useful in various applications such as climbing robots, reusable tapes, supergrip tires, and rapid patch repairs on military vehicles.

For the past decade, extensive efforts have been made to fabricate synthetic gecko foot hairs using polymeric fibers and rods (5−13), as well as carbon nanotube (CNT) arrays (14−21). Of particular interests are the hierarchical fibrillar nanostructures that can achieve anisotropic adhesives for readily switch between strong attachment and easy detachment. Most recently, Qu et al. (22) created gecko-foot-mimetic dry adhesives that show macroscopic adhesive force of ∼100 N/cm^2, which is almost 10 times that of a gecko's foot, and a feature of much stronger shear force (friction) than normal force (adhesion) ensures strong binding along the shear direction and easy lifting in the normal direction. They accomplished this by using a CNT array that was dominated by a straight vertically aligned body-segment along with laterally distributed tips at the top. Such anisotropic adhesives are also achieved in polymeric fibrillar systems (13).

Understanding of the adhesive anisotropy in hairy structures is of great importance for the design and fabrication of switchable dry adhesives. Although theoretical analyses have been made both on the friction and adhesion force of gecko's foot hairs (2, 23−30) and synthetic adhesive materials (31−34), most of them were focused on single seta or single micro/nanofiber. The issues, such as gripping and releasing mechanisms, the hierarchical structure to increase real contact, ideal tip shape, fiber size, aspect ratio, tilted angle, and mechanical properties, have been studied mostly for polymer based synthetic materials. Also there are several numerical models proposed by different research groups (35−39) to investigate adhesive behaviors of single seta. However, the complex fiber−fiber interactions and dynamics of the fiber array, which may significantly influence the behavior of the synthetic adhesives, have not been investigated. Specifically, the vertically aligned CNT array with laterally distributed tips has not been fully analyzed in spite of their excellent performance. Moreover, the transition of the adhesive force from microlevel to macrolevel has not been well understood yet. In this study, a hierarchical multiscale modeling approach is proposed to analyze the adhesive behaviors of the CNT-based hierarchi-

* Corresponding author. E-mail: zxia@uakron.edu.
Received for review May 10, 2010 and accepted July 28, 2010

DOI: 10.1021/am100409s

Published on Web 08/13/2010

cal fibrillar structures. A coarse grained molecular dynamics (CGMD) simulation was performed at the microlevel to analyze the effects of the laterally distributed segments on friction and adhesion strengths. The relationships between the adhesive force and displacement obtained in CGMD simulation were input as cohesive laws into a finite element model (FEM) with a layer of cohesive zone to analyze the device-level CNT-based dry adhesives. The results show that the laterally distributed CNT segments play an important role in achieving strong binding along the lateral direction and weak adhesion in normal direction. The predictions were compared with experimental data of vertically aligned CNT array with laterally distributed segments, and revealed an important mechanism of friction-enhanced adhesion, similar to that found in gecko feet. The modeling provides a direction for optimizing the biomimicking anisotropic adhesives.

2. MODEL DESCRIPTION

2.1. Molecular Dynamics Models. Coarse-grained molecular dynamics models were developed to simulate the deformation, friction, and adhesion of CNT arrays. With the input from fully atomic simulations or experiments, the CGMD approach can accurately and efficiently simulate fiber-to-fiber and fiber-to-substrate interactions. The present CGMD models consist of 100 hexagonally distributed vertically aligned CNTs with a diameter of $d = 30$ nm and a spacing of $b = 68$ nm, each of which attaches a segment of randomly oriented laterally distributed CNT of certain length at its top. To create the laterally distributed segments, we first generated an entire vertically aligned CNT array of certain height, in which each CNT was divided into two portions. The beads in the upper portion were fixed in all degrees of freedom, whereas those in the lower portion were free in deformation. The nanotube array was then pressed onto a rigid surface. Under the pressing, the lower portion were curved and completely contact the target surface on their sides. Finally, the bond length and bending angles of the beads in the deformed configuration were used as initial parameters to form the aligned CNT array with lateral segments. The deformed configuration was fully relaxed and then taken as the initial state of the hierarchical CNT structures. Figure 1 shows the initial state of a CNT array with 600 nm lateral segments on a target surface, modeled as chains of beads. Each bead represents a CNT segment with an aspect ratio $L/d = 1$. The target surface was modeled as an analytical plan and is not shown in Figure 1. Note that the initial state of the CNT array shown in Figure 1 is in a free state without applying any external load or boundary conditions.

The general expression of total steric potential energy, in molecular dynamics, is the sum of energies due to valence or bonded interactions and nonbonded interactions between the beads, which is given in eq 1

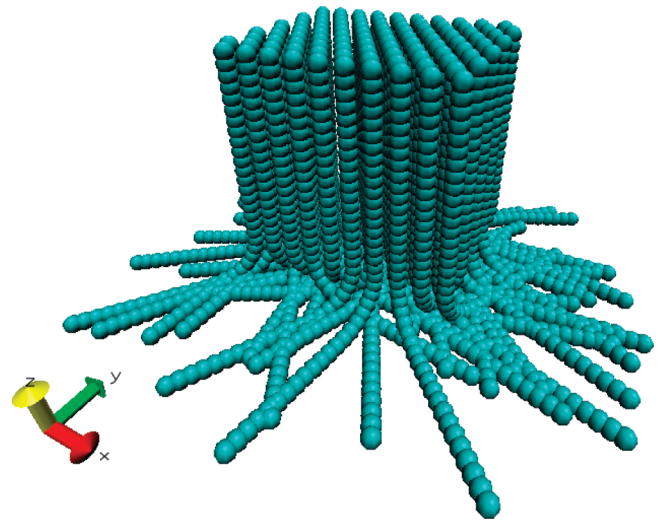

FIGURE 1. Initial configuration of 100 hexagonally distributed vertically aligned CNTs with 600 nm laterally distributed segments represented by beads.

$$U = \sum \frac{1}{2}k_s(l - L)^2 + \sum \frac{1}{2}k_b(\theta - \Theta)^2 + \sum \frac{1}{2}k_t(\phi - \Phi)^2 + \sum U_V \quad (1)$$

where the first three terms on the right-hand side of eq 1 represent the potential energies for the stretching with bond length l and original bond length L, bending with bending angle θ and original angle Θ, and torsion with torsional angle φ and original angle Φ between bonded beads, respectively, as schematically shown in Figure 2. k_s, k_b, and k_t in eq 1 are the corresponding constants of stretching, bending, and torsion, respectively. On the basis of structural mechanics, only three stiffness parameters need to be determined for deformation analysis of CNTs, because of their rounded cross-sections. These parameters are tensile stiffness (EA), bending stiffness (EI), and torsional rigidity (GJ). The energy principle leads to a direct relationship between the parameters within structural mechanics and the force field constants of molecular mechanics (40). It can be established as $k_s = EA/l$, $k_b = EI/l$, and $k_t = GJ/l$, where l is the distance between the centers of each bead the same as the bond length in eq 1. In this study k_t is set to be zero. The potential in eq 1 leads to a linear model which is accurate in describing relatively small CNT deformations. For large deformations, more accurate models exist (41, 42).

The parameters used in eq 1 were derived from a fully atomistic simulation (43−46). Interested readers should consult refs 43 and 44 for computational details. Briefly, an ideal multiwalled carbon nanotube of the desired length and diameter was generated. Molecular dynamics was used to simulate the stretching, bending and buckling behaviors using Brenner potential (47). Young's modulus, bending stiffness of the nanotube were then abstracted from the simulations.

The last term in eq 1 represents the potential energy of interactions between nonbonded beads (fiber−fiber interaction), and those between beads and target surface (fiber−

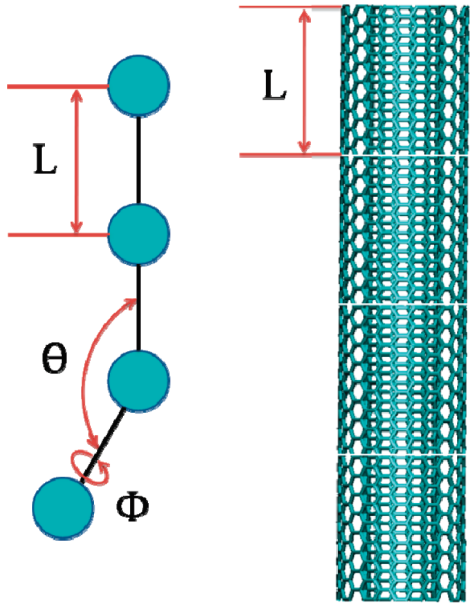

FIGURE 2. Beads and small segments of a fully atomistic nanotube. Each bead represents a small segment of the nanotube.

target surface interaction). These interactions are realized by introducing van der Waals forces between the beads and the "imaginary" target surface. The fiber−target surface interaction potential is determined by integrating the Lennard−Jones potential and can be approximated as

$$U(r) = \pi^2 \rho_c \rho_t R\left[\frac{A}{1260r^7} - \frac{B}{6r}\right] \quad (2)$$

where A and B are Lennard−Jones parameters ($A = 4er_0^{12}$, $B = 4er_0^6$, where $e = 2.286$ meV, and $r_0 = 3.468$ Å for carbon materials (46)), R is the nanotube radius, r is the distance between the bead and target surface, and ρ_c and ρ_t are the density of CNT and the target surface ($\rho_c = \rho_t = 2.0$ g/cm^3), respectively. The fiber−fiber interaction potential takes the same form as eq 2, with ρ_t and r replaced by the density of CNT and fiber−fiber distance, respectively.

Because the target surface is simplified as an analytical surface, the frictional force F_f between the CNT beads and the surface is introduced by the friction law:

$$F_f = \mu F_\perp = \mu\pi^2 \rho_c \rho_t R\left(\frac{A}{180r^8}\right) \quad (3)$$

where $F_\perp$ is the normal force on the target surface and μ is the friction coefficient ($\mu = 0.2$ is assumed in this study) between the beads and the target surface. The direction of the frictional force on a bead is always in opposite direction of the total force (excluding the frictional force) on the bead. During the simulations, if the frictional force calculated based on eq 3 is larger than the total force on a bead, the frictional force is set equal to the force but in the opposite direction, such that the bead is kept in the same position because of static friction.

During MD simulation, the upper two layers of the beads of the vertically aligned CNTs were dragged laterally or pulled normally with respect to the target surface at a constant speed of 3.64 m/s, which is generally sufficient to reach a near-equilibrium structure at a temperature of 300 K. The overall loading displacement was set up to 0.3 μm in each direction. Periodical boundary conditions were applied on the CNT array in x- and y-directions (Figure 1).

2.2. Finite Element Models. Two dimensional finite element models were generated to simulate the macrolevel friction and adhesion of the CNT array with the same dimension (4 × 4 mm^2) as the experimental samples reported in ref 22. Software package Abaqus 6.8−2, was used to perform the finite element analysis (FEA). The finite element models consist of four parts: a cohesive zone, a number of vertical beams, a horizontal beam, and an analytical plane, representing laterally distributed CNTs, vertically aligned CNTs, substrate, and target surface, respectively, as schematically shown in Figure 3.

Specifically, friction and adhesion behaviors of CNT array at the macrolevel were treated as the fracture resistance of a cohesive layer. Thus, a cohesive zone model was adopted to simulate the interactions between the laterally distributed CNTs and the target surface. This cohesive zone features distinct traction−separation relations in pure shear and pure normal directions, and a layer of cohesive elements serves as an interface or path for crack initiation and propagation. The bilinear traction−separation laws, as shown in Figure 4, were derived from MD simulation discussed in section 3.1. Equation 4 describes the normal traction−separation law of each cohesive element. The traction−separation response in shearing direction takes the same form as eq 4, except the subscripts being changed from n to s.

$$T_n = \frac{T_n^0}{\delta_n^0}\delta_n \text{ when } 0 \le \delta_n \le \delta_n^0$$

$$T_n = \frac{T_n^0}{\delta_n^f - \delta_n^0}(\delta_n^f - \delta_n) \text{ when } \delta_n^0 < \delta_n \le \delta_n^f \quad (4)$$

where T_n^0 is the normal cohesive strength, δ_n^0 is the normal displacement jump between two cohesive surfaces when damage initiates, and δ_n^f is the normal displacement jump when separation completes. In our simulation, the δ_n^0 and δ_s^0 are controlled by $E_c = T_n^0/\delta_n^0$ and $G_c = T_s^0/\delta_s^0$, respectively.

The vertical aligned CNTs were modeled by 101 vertical beams with a spacing of 40 μm. Each beam represents a number of vertically aligned CNTs. The effective mechanical properties of the beam were calculated from an array of 5−6 layer multiwall CNTs with an outer diameter of $d = 15$ nm, density of $\rho = 5 \times 10^{10}$ tube/cm^2, and Young's modulus of 1040 GPa. The effective cross section (radius) of the beams was calculated as $S = \sim 362$ nm for a straight CNT array with no interaction between CNTs. However, the CNTs in the synthetic adhesives are not perfectly straight and contact with each other, which could significantly increase the bending stiffness of the CNT array. To include the effect of

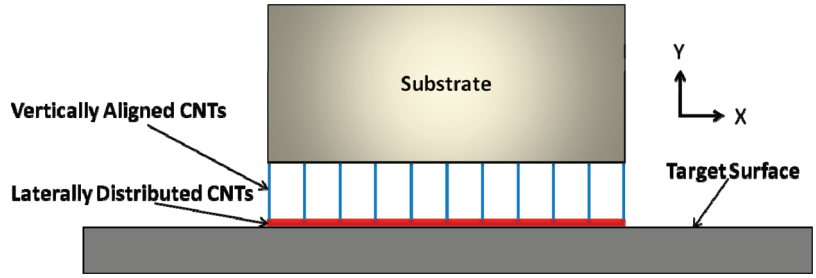

FIGURE 3. Schematic of the CNT-based dry adhesive pad contacting a target surface.

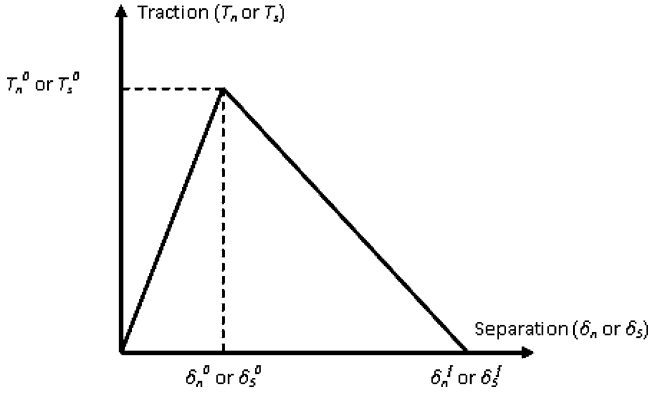

FIGURE 4. Typical traction−separation responses used in FEA simulations.

fiber−fiber contact, we obtained the effective radius of the beams by fitting the height of deformed samples under shear loading. The effective radius of the beams could be described as $S = -2.8 \times 10^{-5}h^2 + 0.021h + 0.25$, ($h = 5-150$ μm), where h is the height of the vertical beams. Each vertical beam was meshed into a number of three-node beam elements, and each element at its bottom shares a node with the cohesive elements.

The substrate was modeled by one horizontal beam with a length of 4000 μm, and a rectangular cross section with an out-of-plane thickness of 4000 μm and a height of 380 μm. The horizontal beam was meshed into 100 two-node beam elements, and the nodes were sheared by the top nodes of the vertical beams. The bottom surface of the cohesive zone represents the target surface, the nodes of which were constrained in all translational degrees of freedom.

3. RESULTS

3.1. Friction and Adhesion at the Microscale.

Figure 5 shows the snapshots of the CNT array with 360 nm laterally distributed segments under shear and normal loadings. When the array is subject to normal loading, the CNTs is lifted, causing sudden peeling of the laterally distributed segments from the target surface, i.e., a series of beads that contact the surface are successively lifted from the surface. After peeling, as shown in snapshots b and c in Figure 5, the beads at the ends still contact the target surface but each segment has only one bead at the tip contacting the surface. While the laterally distributed segments are gradually pulled straight, the tip beads slide along the target surface and are eventually pulled off simultaneously. As the CNT array being loaded in shear direction, the randomly oriented CNT segments are pulled almost straight along the lateral direction (Figure 5e−h) because of their interactions with the target surface. The vertically aligned CNT "trunks" are also tilted toward the shear loading direction to an extent. These phenomena are consistent with the experimental observations in ref 22.

Normal and shear stresses between the laterally distributed CNTs and target surface were calculated for various lengths of the lateral segments, and the stresses versus displacement curves were plotted in Figure 6. As shown in Figure 6a when the length of the laterally distributed segments is longer than a certain value (e.g., 360 nm), the frictional force increases almost linearly to a maximum value (failure initiation point) and then decreases slowly (failure evolution process). Our observations on the deformation of CNT array, during shear loading, show that the peak is caused by the adjustment of the orientations of the laterally distributed segments. Longer laterally distributed segment results in higher peaks and also higher fracture energy (area under each curve). For the case of the laterally distributed segments less than 360 nm, the frictional stress increases slowly, and there is no obvious peak generated during the loading. This suggests that for short laterally distributed CNTs, the friction due to the orientation adjustment is not large enough to generate a peak.

Figure 6b shows the normal adhesion behaviors of CNT array with different length of laterally distributed segments. For a given laterally distributed length, there is a peak stress at the displacement of approximately 2−5 nm, followed by a secondary peak. The displacement at which the secondary peak occurs becomes larger as the laterally distributed length increases. The first peak stresses are lower than the secondary ones. As the length of laterally distributed segments increases, the altitude of the first peak increases and then decreases, whereas the height of the secondary peaks are nearly constant. The presence of duel peaks is due to the unique deformation mechanisms during normal loading. As described before, when a normal displacement is applied to the CNT array, the laterally distributed segments will be peeled off at the first stage. Because the peeling is a crack propagation process, all the beads, except for the beads at the tip of the laterally distributed segments, are rapidly pulled off the target surface consecutively from the stem toward the tip. This process generates the first peak which depends on the laterally distributed segments. After peeling, the tip beads, which are still in contact with the target surface, undergo a sliding along the target surface. Finally,

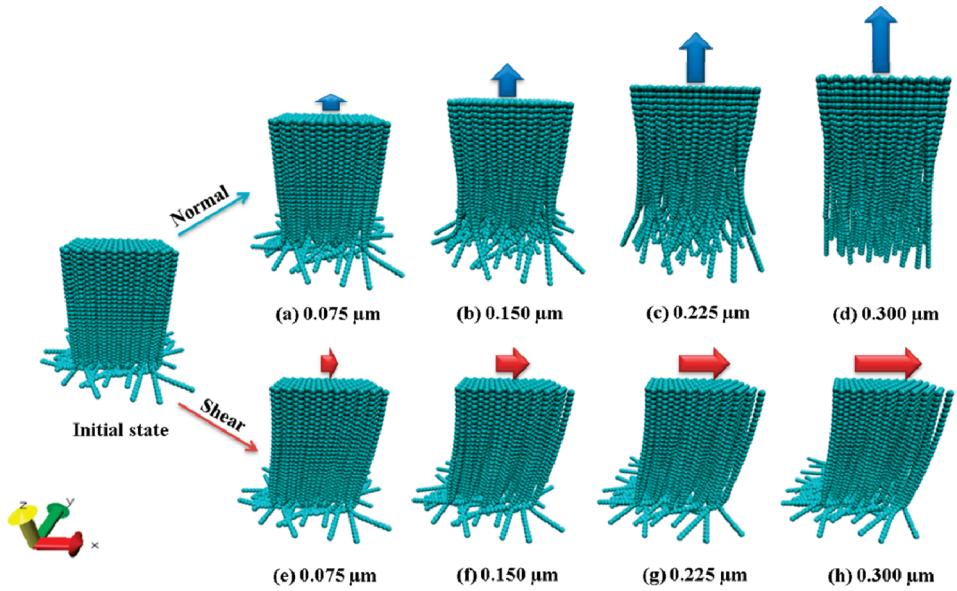

FIGURE 5. Snapshots of the CNT array with 360 nm laterally distributed segments under (a–d) normal loading and (e–h) shear loading.

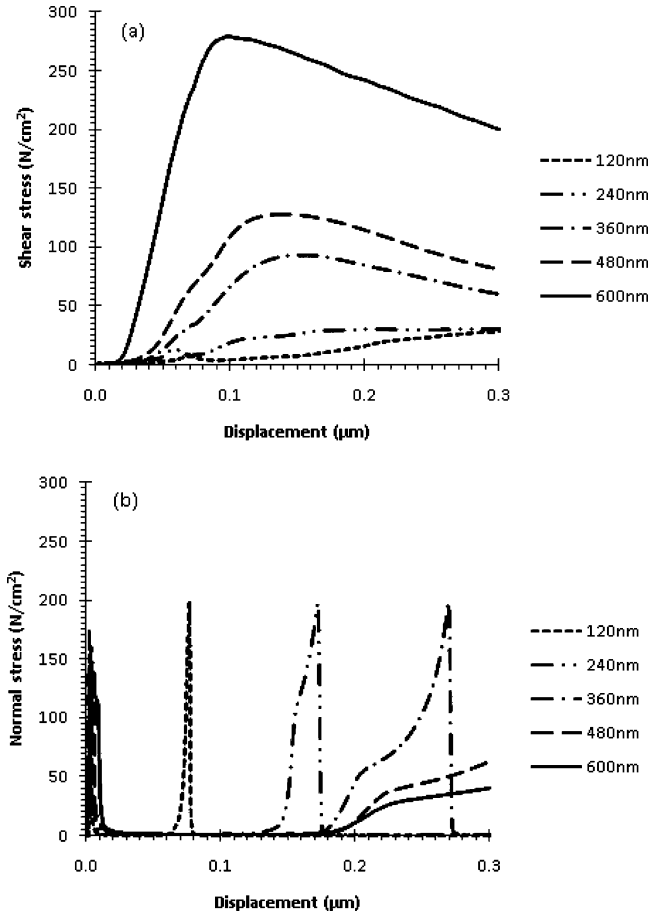

FIGURE 6. (a) Shear and (b) normal stresses of CNT arrays with different length of laterally distributed segments. The numbers in the legends represent the lengths of the laterally distributed segments.

the separation between the last beads and the target surface generates the second peak in the traction–displacement curves. CNT array with longer lateral segment would need larger applied displacement to be pulled off. Thus, for longer laterally distributed CNTs, the secondary peak appears at larger displacements. Fracture energy, mainly due to the secondary peak, becomes larger as the length of laterally distributed segments increases but the height of the secondary peak almost remains constant because the same separation mechanism occurs. From the above analysis, it is clear that the first peak is due to the peeling, whereas the secondary peak is caused by the separation of the tip beads from the target surface.

It should be noted that friction and adhesion behaviors shown in Figure 6 are the collective effects of 100 nanotubes with the same length of laterally distributed segments. In reality, the length of the laterally distributed segments may vary within the same array. To account for the effect of the length variations, one can simply use the same procedure described above to compute the shear and normal stresses by varying the length of the laterally distributed segments within the array. This, however, requires developing largescale models to include the effect of the length distribution. Instead of performing such a largescale simulation, here, we assume that the probability $p(x)$ of certain length of the laterally distributed segments in a CNT array can be described by a Gauss distribution

$$p(x) = \frac{1}{(\mathrm{SD})\sqrt{2\pi}}\exp\left(-\frac{(x-m)^2}{2(\mathrm{SD})^2}\right) \quad (5)$$

where x, m, and SD are certain length of the laterally distributed segments, mean, and standard deviation, respectively. The effective stress or traction in normal or shear direction ($T_{n,s}$) can be calculated by integrating eq 5 with respect to laterally distributed length

$$T_{n,s} = \int_0^\infty p(x)\sigma_{n,s}(x,\delta)dx \quad (6)$$

where $\sigma_{n,s}(x,\delta)$ represents the normal or shear stress calculated using CGMD simulation for certain laterally distributed

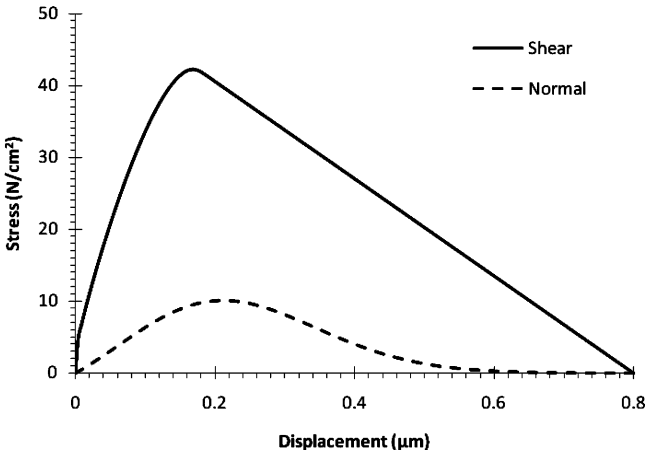

FIGURE 7. Effective stress and displacement curves under shear and normal loadings, derived by combination of MD simulation results and normal distribution of the laterally distributed length, where $m = 135.38$ nm and SD $= 240.11$ nm.

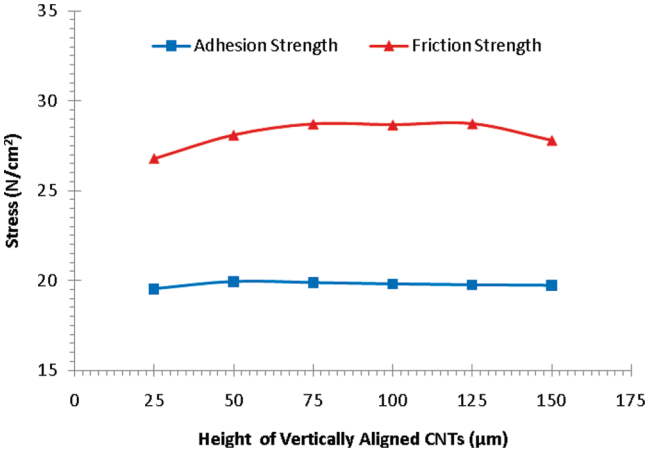

FIGURE 8. Friction and adhesion strengths as a function of the height of vertically aligned CNTs h, where $T_n^0 = 0.2$ MPa, $T_s^0 = 0.8$ MPa, $E_c = 0.5$ MPa/μm, $G_c = 2$ MPa/μm, and $\delta_n^f = \delta_s^f = 3.0$ μm.

length (x) at certain displacement (δ) under normal or shear loading. $\sigma_{n,s}(x,\delta)$ can be obtained by interpolating the data from Figure 6. The results derived are the effective stress-displacement curves in shear or normal direction with respect to certain normal distribution parameters, mean (m) and standard deviation (SD). Figure 7 shows an example of the effective stress as a function of displacement under shear and normal loadings, where $m = 135.38$ nm and SD $=$ 240.11 nm. The first peak effect was neglected in the calculation of the normal stress due to the domination of the secondary peak for breaking the fiber−target surface interactions. The effective stress-displacement curves can be used as an appropriate input for the traction−separation law in FEA.

3.2. Friction and Adhesion at the Device Level.

We first investigated the effect of the vertically aligned CNTs on the friction and adhesion strength. Figure 8 shows the friction and adhesion of the adhesive pads in FEA, with a fixed length of laterally distributed CNT segments x, but different height of the vertically aligned CNT array h. The adhesion is almost independent of h, whereas the friction slightly changes with an increase in h.

The above results are attributed to the distinct deformation mechanisms of the adhesive pads under normal and shear loadings. The CNT array is highly anisotropic materials, which is stiff in axial direction but much compliant in transverse direction. The vertically aligned CNT array is highly curved under shear loading, as shown in Figure 9b. The shear loading also induces a bending moment on the CNT array, which depends on the height of the array. As a result, the cohesive elements are subjected to both normal and shear forces, and the adhesives may fail in normal direction since the normal force may exceed the normal cohesive strength T_n^0. With an increase of the height of vertically aligned CNTs, the normal force acting on the cohesive zone increases, leading to the reduction of the friction strength because the normal failure of the cohesive elements occurs before shear failure. However, increasing shear loading also reduces the effective height of the CNT array due to its curving-down deformation, which reduces the bending moment or normal force on the cohesive elements. These two factors are almost canceled out during shear loading, making the friction less sensitive to the height of the vertically aligned CNTs. On the other hand, during normal loading, the whole adhesive pad is stretched uniformly (Figure 9c) and the change in the height of vertically aligned CNTs does not affect the deformation of the cohesive elements.

The effect of the laterally distributed CNTs (described by the traction−separation laws) on friction and adhesion behaviors were studied by adjusting the cohesive parameters for a given height of vertically aligned CNT array ($h = 100$ μm). There are totally 6 parameters (T_n^0, δ_n^0, and δ_n^f in normal direction, and T_s^0, δ_s^0, and δ_s^f in shear direction) in the bilinear cohesive laws, describing the damage initiation and evolution of the cohesive elements in normal and shear directions. We have studied the influence of δ_n^0 and δ_s^0 on friction and adhesion, and found that the effects of these parameters are trivial. Similar results are obtained for the parameters, δ_n^f and δ_s^f. Figure 10 shows the friction and adhesion of the adhesive pads as a function of shear and normal cohesive strengths, T_s^0 and T_n^0, respectively. For a given T_n^0, the friction linearly increases and then reaches a plateau with an increase of T_s^0, whereas the adhesion remains constant (Figure 10a). The turning point of the friction suggests that there is a transition from shear failure to normal failure mode. As T_s^0 increases to the critical point, the adhesive will fail in normal direction due to the increase of bending moment induced by the shear loading. If T_s^0 is fixed, the adhesion is a linear function of T_n^0, but the friction increases gradually at first and then becomes independent of T_n^0 when T_n^0 exceeds a critical value, as shown in Figure 10b. In this case, an opposite transition of failure modes from normal to shear occurs at this critical value. From the above parametric studies, it is obvious that among all the parameters in CNT array, the cohesive strengths T_s^0 and T_n^0 are the dominating parameters in determining the macroscale friction and adhesion of the nanotube array. Because T_s^0 and T_n^0 are directly related to the laterally distributed segments of the CNT array, the combination of

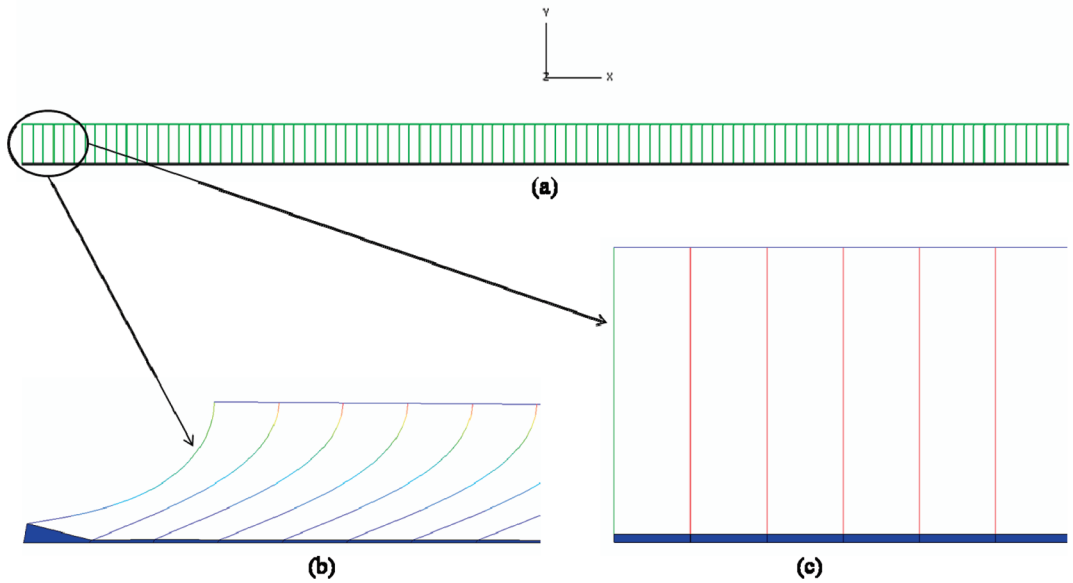

FIGURE 9. Snapshots of FEA-predicted deformation of vertically aligned CNT array with $h = 150\ \mu$m: (a) at initial state, (b) under shear loading, and (c) under normal loading.

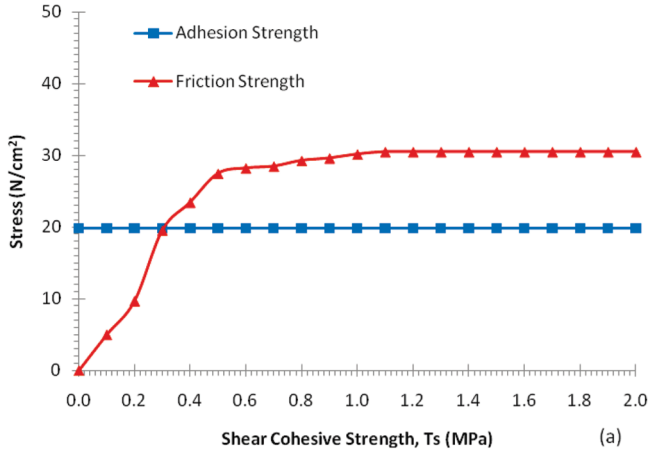

FIGURE 10. Effect of cohesive law parameters: (a) T_s^0 for $T_n^0 = 0.2$ MPa, and (b) T_n^0 for $T_s^0 = 0.8$ MPa, on the friction and adhesion strengths for $E_c = 0.5$ MPa/μm, $G_c = 2$ MPa/μm, $\delta_n^f = \delta_s^f = 3\ \mu$m and, $h = 100\ \mu$m.

CGMD and FEA enables us to link the nanoscale structures of the dry adhesives to their macroscale friction and adhesion performance.

4. DISCUSSION

The numerical analyses presented in section 3 suggest that the cohesive laws in shear and normal directions represent the friction and adhesion properties at the microscale, and provide a bridge to correlate the interfacial microstructure with the macroscale performance of the CNT based adhesives. Thus, the interfacial structures and in situ adhesive properties of the CNT array could be estimated from the parameters of the traction−separation relationships and the CGMD simulation results. We now utilize this bridge to analyze the friction and adhesion behaviors of the hierarchical CNT based adhesives reported in ref 22.

We first consider how the nanoscale structure and properties are related to macroscale adhesion of the adhesives. The normal cohesive strength T_n^0 for the dry adhesives can be determined from the FEA models by fitting the experimental data. On the other hand, maximum adhesion force per unit area P_{max}, generated by the interaction between CNTs and target surface, can be calculated using microscale interfacial interaction models. Because the same interfacial force is calculated from different approaches, the normal cohesive strength should be equal to the maximum adhesion force per unit area $T_n^0 = P_{max}$. According to the CGMD simulation, the maximum adhesion force is the result of the nanotubes contacting with the target surface at their top ends. Thus, the maximum adhesion force per unit area can be calculated by eq 2, which is simplified as $P_{max} = \rho Cd/12r^2$, with the Hamaker constant C, the nanotube diameter d, and the gap distance between the nanotube surface and the target surface r. There is a gap distance $r = r_0$, representing the effective separation between the nanotube and the target surface, at which maximum attractive force P_{max} is achieved. Using the values of $d = 15$ nm, $\rho = 1 \times 10^{10}$ to 1×10^{11} tubes/cm^2, $r_0 = 0.34$ nm and $C = 6.5 \times 10^{-20}$ J, for glass surface (48, 49), the maximum adhesion force is estimated to be $P_{max} = 0.007-0.07$ MPa, which is very close to the

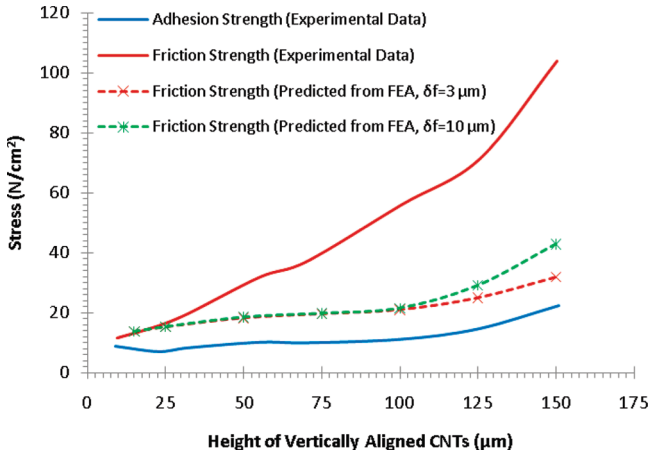

FIGURE 11. Predicted and measured friction and adhesion of CNT dry adhesives with different height of vertically aligned segments. Dashed lines represent the friction strength under shear loading, predicted by FEA using T_n^0 obtained from the fitting under normal loading. By increasing the values of displacement jump defining the complete separation, $\delta^f = \delta_n^f = \delta_s^f$, from 3 to 10 μm, the fracture energy of the cohesive zone increases and predicted adhesion strength increases slightly.

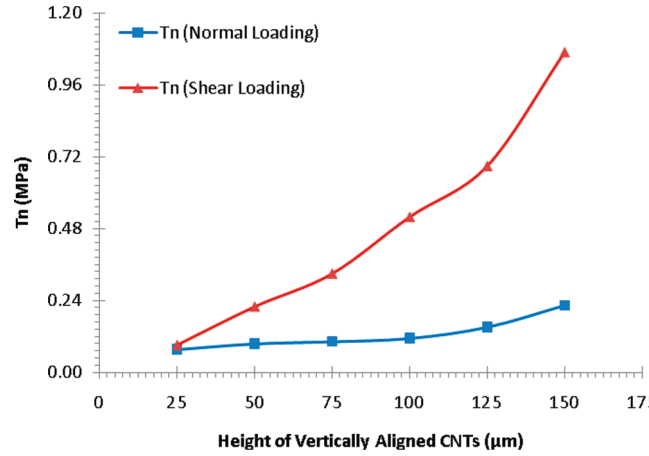

FIGURE 12. Normal cohesive strengths T_n^0 as a function of vertically aligned CNT height, required for fitting the experimental data under normal and shear loadings separately.

normal cohesive strength ($T_n^0 = 0.07-0.22$ MPa) calculated from FEA and fitting.

We further analyze the effect of interfacial nanostructures on the macroscale friction of the dry adhesives. It has been shown from CGMD simulations that the friction is generated by the laterally distributed CNT segments, and the maximum friction force per unit area of the nanotubes, P_f^{max}, should be equal to the shear cohesive strength, T_s^0, which can be calculated with the FEA model by adjusting the shear cohesive strength T_s^0 to fit the experimental friction (Figure 11). However, to our surprise, except for short CNT array, it is impossible to match the experimental results when previously fitted T_n^0 for normal loading is used. As shown in Figure 11, for CNT height larger than 25 μm, the predicted macroscale friction strength starts to divert from the experimental curve, and the difference between them becomes large with the increase of the height of vertically aligned CNTs. We also tried to change other parameters of the traction-separation laws, e.g., changing δ^f, from 3−10 μm, which is considered to be the upper limit because the actual laterally distributed length of the samples are just a couple of micrometers. But still the predicted friction strength could not match the experimental data.

The above unexpected behavior of the friction is attributed to the complex deformation of the CNT array under shear loadings. As demonstrated in section 3.2, the cohesive zone elements (or laterally distributed CNT segments) are subject to not only shear stresses but also normal stresses due to the bending moment induced by the shear loading. When the normal stress on the cohesive elements exceeds their normal cohesive strength T_n^0, failure will occur in the normal failure mode. The simulation results show that the normal failure does occur for the CNT adhesives with a height larger than 25 μm. To match the experimental results (friction), the normal cohesive strength T_n^0 must be increased. In other words, there must be an enhanced adhesion in the biomimetic CNT-based adhesives under shear loading conditions. Such an enhanced adhesion increases with an increase in frictional force.

The phenomena of the enhanced adhesion during shear loading have been observed in gecko adhesives and other frictional systems. Autumn et al. (50) observed that dragging along the natural curvature of setae is necessary to generate sufficient adhesion. They also found that the ratio of the shear reaction force to the normal force remains almost constant, although the magnitude of the force varies. To explain their experimental findings, Autumn et al. (50) proposed a phenomenological frictional adhesion model, which was also adopted by Tian et al. (51) in modeling the adhesion of a spatula pad. Using a generalized Kendall model incorporating the effect of pretension, Chen et al. (52) also show that peel-off force of a thin film from a substrate depends on the magnitude of pretension on the film. The pretension can significantly increase the peel-off force. These observations and analyses suggest that pretension/friction-enhanced adhesion may be a general phenomenon and may also exist in the CNT array although the details of the mechanism remain unclear. We have calculated T_n^0 necessary to match the experimental results under shear loading using the FEA models and found that T_n^0 must be increased by a factor of ~5 compared to the value of T_n^0 under normal loading (Figure 12). Because the strong friction force is mainly generated by the laterally distributed CNT segments at the top of vertically aligned CNT array, the laterally distributed CNT segments must play an important role in enhancing the adhesion. Controlling the morphology of the laterally distributed CNT segments could lead to dry adhesives with improved adhesion and friction. Thus, the multilevel hierarchical structures are critical to achieve high adhesive anisotropy and friction-enhanced adhesion. Our multiscale models link these unique phenomena to the microstructures of synthetic adhesives, providing an insight into the friction and adhesion mechanisms in the biomimicking dry adhesives.

5. CONCLUSIONS

A multiscale modeling approach has been developed to analyze the friction and adhesion of hierarchical fibrillar

adhesives. The models were applied to vertically aligned CNT array (mimicking gecko setae) with laterally distributed CNT segments (mimicking gecko spatulae). Simulation results show that increasing the length of the laterally distributed CNT segments can drastically promote the shearing force, while keeping normal adhesion force almost constant. The laterally distributed CNT segments also strongly enhance the adhesion of the CNT adhesives under shear loadings. Through the multiscale approach, the role of the laterally distributed CNT segments as well as vertically aligned CNT array can be analyzed and linked to the macroscale performance of the dry adhesives. The analysis provides the strategies for biomimetic design of new types of switchable dry adhesives using CNT array.

Acknowledgment. The authors gratefully acknowledge support of this work by NSF under Contract CMMI-0825990.

REFERENCES AND NOTES

(1) Autumn, K.; Liang, Y. A.; Hsieh, S. T.; Zesch, W.; Chan, W. P.; Kenny, T. W.; Fearing, R.; Full, R. J. *Nature* **2000**, *450*, 681–685.
(2) Autumn, K.; Peattie, A. M. *Integr. Comp. Biol.* **2002**, *42*, 1081–1090.
(3) Autumn, K.; Sitti, M.; Liang, Y. A.; Peattie, A. M.; Hansen, W. R.; Sponberg, S.; Kenny, T. W.; Fearing, R.; Israelachvili, J. N.; Full, R. J. *Proc. Natl. Acad. Sci. U.S.A.* **2002**, *99*, 12252–12256.
(4) Irschick, D. J.; Austin, C. C.; Petren, K.; Fisher, R. N.; Losos, J. B.; Ellers, O. *Biol. J. Linnaen Soc.* **1996**, *59*, 21–35.
(5) Geim, A. K.; Dubonos, S. V.; Grigorieva, I. V.; Novoselov, K. S.; Zhukov, A. A.; Shapoval, S. Y. *Nat. Mater.* **2003**, *2*, 461–463.
(6) Kim, S.; Sitti, M. *Appl. Phys. Lett.* **2006**, *89*, 261911.
(7) Kustandi, T. S.; Samper, V. D.; Ng, W. S.; Chong, A. S.; Gao, H. *J. Micromech. Microeng.* **2007**, *17*, N75–N81.
(8) Reddy, S.; Arzt, E.; Campo, A. D. *Adv. Mater.* **2007**, *19*, 3833–3837.
(9) Lee, J.; Fearing, R. S. *Langmuir* **2008**, *24*, 10587–10591.
(10) Lee, J.; Majidi, C.; Schubert, B.; Fearing, R. S. *J. R. Soc. Interface* **2008**, *5*, 835–844.
(11) Davies, J.; Haq, S.; Hawke, T.; Sargent, J. P. *Int. J. Adhes. Adhes.* **2008**, *29*, 380–389.
(12) Murphy, M. P.; Kim, S.; Sitti, M. *ACS Appl. Mater. Interfaces* **2009**, *1*, 849–855.
(13) Parness, A.; Soto, D.; Esparza, N.; Gravish, N.; Wikinson, M.; Autumn, K.; Cutkosky, M. *J. R. Soc. Interface* **2009**, *6*, 1223–1232.
(14) Yurdumakan, B.; Raravikar, N. R.; Ajayan, P. M.; Dhinojwala, A. *Chem. Commun.* **2005**, *30*, 3799–3801.
(15) Zhao, Y.; Tong, T.; Delzeit, L.; Kashani, A.; Meyyapan, M.; Majumdar, A. *J. Vac. Sci. Technol. B* **2006**, *24*, 331–335.
(16) Aksak, B.; Sitti, M.; Cassell, A.; Li, J.; Meyyappan, M.; Callen, P. *Appl. Phys. Lett.* **2007**, *91*, 061906.
(17) Ge, L.; Sethi, S.; Ci, L.; Ajayan, P. M.; Dhinojwala, A. *Proc. Natl. Acad. Sci. U.S.A.* **2007**, *104*, 10792–10795.
(18) Qu, L.; Dai, L. *Adv. Mater.* **2007**, *19*, 3844–3849.
(19) Sethi, S.; Ge, L.; Ci, L.; Ajayan, P. M.; Dhinojwala, A. *Nano Lett.* **2008**, *8*, 822–825.
(20) Wirth, C. T.; Hofmann, S.; Robertson, J. *Diamond Relat. Mater.* **2008**, *17*, 1518–1524.
(21) Maeno, Y.; Nakayama, Y. *Appl. Phys. Lett.* **2009**, *94*, 012103.
(22) Qu, L.; Dai, L.; Stone, M.; Xia, Z. H.; Wang, Z. L. *Science* **2008**, *322*, 238–242.
(23) Gao, H.; Wang, X.; Yao, H.; Gorb, S.; Arzt, E. *Mech. Mater.* **2005**, *37*, 275–285.
(24) Takahashi, K.; Berengueres, J. O. L.; Obata, K. J.; Saito, S. *Int. J. Adhes. Adhes.* **2006**, *26*, 639–643.
(25) Tian, Y.; Pesika, N.; Zeng, H.; Rosenberg, K.; Zhao, B.; McGuiggan, P.; Autumn, K.; Israelachvili, J. *Proc. Natl Acad. Sci. U.S.A.* **2006**, *103*, 19320–19325.
(26) Yao, H.; Gao, H. *J. Adhes. Sci. Technol.* **2007**, *21*, 1185–1212.
(27) Bhushan, B. *J. Adhes. Sci. Technol.* **2007**, *21*, 1213–1258.
(28) Zhao, B.; Pesika, N.; Rosenberg, K.; Tian, Y.; Zeng, H.; McGuiggan, P.; Autumn, K.; Israelachvili, J. *Langmuir* **2007**, *24*, 1517–1524.
(29) Chen, B.; Wu, P. D.; Gao, H. *Proc. R. Soc. London, Ser. A* **2008**, *464*, 1639–1652.
(30) Yamaguchi, T.; Gravish, N.; Autumn, K.; Creton, C. *J. Phys. Chem. B* **2008**, *113*, 3622–3628.
(31) Hui, C. Y.; Glassmaker, N. J.; Tang, T.; Jagota, A. *J. R. Soc. Interface* **2004**, *1*, 35–48.
(32) Spolenak, R.; Gorb, S.; Arzt, E. *Acta Biomater.* **2005**, *1*, 5–13.
(33) Aksak, B.; Murphy, M. P.; Sitti, M. *Langmuir* **2007**, *23*, 3322–3332.
(34) Greiner, C.; Spolenak, R.; Arzt, E. *Acta Biomater.* **2008**, *5*, 597–606.
(35) Cho, Y. S.; Han, H.; Kim, W. D. *J. Bionic Eng.* **2006**, *3*, 209–216.
(36) Gao, H.; Wang, X.; Yao, H.; Gorb, S.; Arzt, E. *Mech. Mater.* **2005**, *37*, 275–285.
(37) Bhushan, B.; Peressadako, A.; Kim, T. W. *J. Adhesion Sci. Technol.* **2006**, *20*, 1475–1491.
(38) Zhao, B.; Pesika, N.; Zeng, H.; Wei, Z.; Chen, Y.; Autumn, K.; Turner, K.; Israelachvili, J. *J. Phys. Chem. B* **2009**, *113*, 3615–3621.
(39) Sauer, R. A. *Comput. Methods Appl. Mech. Eng.* **2009**, *12*, 627–640.
(40) Li, C.; Chou, T. W. *Mech. Mater.* **2004**, *36*, 1047–1055.
(41) Arroyo, M.; Belytschko, T. *J. Mech. Phys. Solids* **2002**, *50*, 1941–1977.
(42) Qian, D.; Wagner, G. J.; Liu, W. K. *Comput. Methods Appl. Mech. Eng.* **2004**, *193*, 1603–1632.
(43) Xia, Z. H.; Liang, J. *Mater. Res. Soc. Symp. Proc.* **2007**, *975*, DD10–09.
(44) Xia, Z. H.; Guduru, P.; Curtin, W. A. *Phy. Rev. Lett.* **2007**, *98*, 245501.
(45) Sears, A.; Batra, R. C. *Phys. Rev. B* **2006**, *73*, 085410.
(46) Xia, Z. H.; Curtin, W. A. *Phys. Rev. B* **2004**, *69*, 233408.
(47) Brenner, D. W. *Phys. Rev. B* **1990**, *42*, 9458–9471.
(48) Leckband, D.; Israelachvili, J. *Q. Rev. Biophys.* **2001**, *34*, 105–267.
(49) Huber, G.; Mantz, H.; Spolenak, R.; Mecke, K.; Jacobs, K.; Gorb, S. N.; Arzt, E. *Proc. Natl. Acad. Sci. U.S.A.* **2005**, *102*, 16293–16296.
(50) Autumn, K.; Dittmore, A.; Santos, D.; Spenko, M.; Cutkosky, M. *J. Exp. Biol.* **2006**, *209*, 3569–3579.
(51) Tian, Y.; Pesika, N.; Zeng, H.; Rosenberg, K.; Zhao, B.; McGuiggan, P.; Autumn, K.; Israelachvili, J. *Proc. Natl. Acad. Sci. U.S.A.* **2006**, *103*, 19 32019 325.
(52) Chen, B.; Wu, P.; Gao, H. J. R. *Soc. Interface* **2009**, *6*, 529–537.

AM100409S